



Impact of particle passage and focusing from micro-pore optics for radiation damage estimates

Michael W. J. Hubbard ^{a,*} Thomas W. Buggiey ^a David Hall,^a Charly Feldman ^b
Jonathan Keelan,^a Oliver Hetherington,^a Steven Parsons ^a Timothy Arnold,^a
and Andrew Holland^a

^aThe Open University, School of Physical Sciences, Centre for Electronic Imaging, Milton Keynes,
United Kingdom

^bUniversity of Leicester, School of Physics and Astronomy, Leicester, United Kingdom

ABSTRACT. Space observatories utilizing micro pore optics (MPOs) have been used and are planned for several future X-ray astronomy space missions. The optical systems are designed to facilitate the focusing of incoming photons onto the focal plane of telescopes. Unfortunately, as well as having a small solid angle “open” to the sky, MPOs also have the unintentional effect of focusing high-energy particles from the space radiation environment. This causes additional radiation damage to mission-critical imaging sensors with solar energetic particles being particularly focusable. Typically, processes such as sectoral analysis are used to estimate the predicted dose to components, which is a ray tracing approach, and does not include focusing effects. We investigated focused dose estimation techniques for MPOs using Monte Carlo (MC) simulations. The focused dose contribution was compared with the unfocused contribution for the Solar wind Magnetosphere Ionosphere Link Explorer mission. The unfocused dose estimates were calculated using a traditional sectoral shielding analysis. The Monte Carlo-focused dose simulations enabled dose mapping over the image sensor to be analyzed. This revealed a relatively uniform dose across the device with some focusing artifacts present. The simulations also showed that the total ionizing dose and total non-ionizing dose decreased with depth into the sensor from the entrance window. This is key when considering that charge is often stored at varying depths in imaging devices across different technologies, for example, in front or back illuminated devices.

© The Authors. Published by SPIE under a Creative Commons Attribution 4.0 International License. Distribution or reproduction of this work in whole or in part requires full attribution of the original publication, including its DOI. [DOI: [10.1117/1.JATIS.10.3.034003](https://doi.org/10.1117/1.JATIS.10.3.034003)]

Keywords: Monte Carlo methods; device simulation; micro pore optics; radiation dose; X-ray imaging; X-ray astronomy

Paper 23144G received Dec. 5, 2023; revised Jun. 13, 2024; accepted Jul. 9, 2024; published Aug. 10, 2024.

1 Introduction

Large-area charge-coupled devices (CCDs) are planned to be key components for instruments in future space missions in the next decade. The European Space Agency (ESA) missions such as the Solar wind Magnetosphere Ionosphere Link Explorer (SMILE)¹ and PLANetary Transits and Oscillations of stars (PLATO)² will use these large area CCD technologies to achieve their demanding science goals, in both the X-ray and optical regimes. Future missions will also use large area format image sensors, such as the Transient High-Energy Sky and Early Universe Surveyor (THESEUS) Soft X-ray Imager (SXI),³ which will use complementary metal oxide semiconductor (CMOS) detectors. Although CCD technology can perform well in the

*Address all correspondence to Michael W. J. Hubbard, michael.hubbard@open.ac.uk

radiation-hard space environment and CMOS image sensors even more so, the performance of the device will be significantly degraded over the science lifetime of each mission. To mitigate and understand the effects of both total non-ionizing dose (TNID) and total ionizing dose (TID) radiation damage, pre-flight irradiation campaigns are essential to predicting in-orbit device performance. To facilitate accurate pre-flight irradiation testing, a range of simulations are required, depending on the maturity of the instrument in question. For early-stage instruments, such as those planned for the TreeView mission,⁴ which would observe and monitor tree health from low Earth orbit, a simple spherical shell model is used to estimate an initial dose. This is because the method is the most time efficient and yields relatively accurate results given the early stage of the instrument and mission designs. For more mature instrument designs, such as SMILE SXI⁵ and THESEUS SXI,⁶ sectoral shielding analysis⁷ can be used and can provide a more physical model, and it can often improve the accuracy of dose estimates in comparison with shell models. As designs further mature, a Monte Carlo approach is then used, which is the most time-consuming and computationally intensive method.

Specifically, in the X-ray band, the emergence of new technologies, such as micro pore optics (MPOs), means that there is an ever-increasing open solid angle from space to the focal plane of instruments. This open angle and optical design mean that much lower energy particles can reach the focal plane of an instrument and potentially increase the dose received. The simple spherical shell models and sectoral shielding analysis described above cannot accurately deal with this low-energy component as it is incorrectly removed by equivalent aluminum thickness shielding. Therefore, a full Monte Carlo approach is required to take into account the lower energy component and accurately predict in-orbit doses for instruments that use this new type of X-ray optic. The need for such simulations is further necessitated by the focusing of soft protons by new X-ray optics, which has been observed in past X-ray missions such as X-ray Multi-Mirror (XMM) Newton.⁸ Charged particles such as soft protons can undergo multiple Coulomb scatters when traversing X-ray optical systems leading to focusing.⁹ This has been explored in the past on Wolter optics systems.^{10–12}

This paper explores the contribution to the dose from particles entering via the MPOs of the SMILE spacecraft. The SMILE mission is a collaboration between the European Space Agency (ESA) and the Chinese Academy of Sciences (CAS). SMILE features four key instruments and aims to study the interactions between the solar wind and magnetosphere. One of the instruments is a compact wide-field lobster-eye telescope called the SXI. The SXI features two CCD 370s that are back illuminated. The instrument will study the solar wind charge exchange (SWCX) process by analyzing soft X-rays that are focused by the MPOs. The optics will also focus on soft charge particles and is equipped with a radiation shutter door to protect the CCDs from radiation damage. The door closes when close to Earth to protect from the Van Allen belts and during high SEP flux from high solar activity.

The results presented are from a mission design study referred to as SXI 1.x. The SXI 1.x has a mission profile of a highly elliptical orbit with a mission duration of 3 years and a launch date in April 2022. The sectoral shielding analysis (SSA) is used with depth dose curves to produce dose estimates for the mission. Additionally, Monte Carlo (MC) simulations are used to calculate the dose from focused particles through MPOs, in a lobster eye optic configuration, onto the instrument focal plane. Although SMILE's large-area CCDs are the focus of this publication, this approach will be necessary for accurate dose estimates of all future instruments that use micro pore optics in the X-ray regime, such as the THESEUS mission concept.

2 Micro-Pore Optics

Biomimicry of crustaceans' eyes, specifically lobsters, has inspired the development of a next-generation X-ray optic design.^{13,14} This optical system, referred to as lobster eye optics, is formed by tessellating a number of individual spherically slumped MPOs over a frame with the same radius of curvature. Each MPO is made up of a large quantity of repeating, evenly spaced square pores, which when slumped, all point toward the center of curvature.^{15–17} The pores have a narrow deflection angle for soft X-rays, which is achieved by having a high-quality X-ray reflective coating on the pores' internal surfaces and a high ratio between the pore length and pore width.^{18,19} An example of these dimensions is shown for a small MPO array in Fig. 1(a).

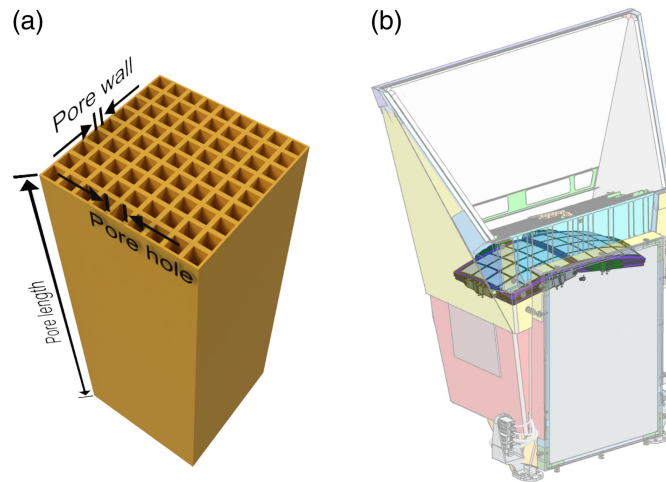


Fig. 1 Example of MPOs used for instrumentation on the SMILE mission and example of key parameters used for design. (a) Example of a small MPO array with key dimensions labeled. (b) SMILE SXI with a lobster eye MPO array.

Table 1 Parameters used in calculations for the focused dose through lobster eye optics.

Parameter	Value
Lobster eye focal length	300 mm
MPO pore hole width	40 μm
MPO pore wall width	12 μm
MPO pore length	1.2 mm
CCD side length	81 mm
CCD thickness	16 μm

MPOs are made of lead glass and are usually coated with iridium.^{20,21} The radius of curvature of the individual MPOs, and therefore the slumped metal frame, is selected depending on the instrument/mission science requirements. An example of MPOs integrated into the design of the SMILE Soft X-ray Imager (SXI) spacecraft is shown in Fig. 1(b). MPOs have a high technology readiness level, are currently being flown on the mercury imaging X-ray spectrometer (MIXS) instrument for BepiColombo,²² and are being used for the SMILE SXI²¹ and the microchannel X-ray telescope (MXT) instrument on the space variable objects monitor (SVOM)²³ mission, among others.^{24,25} In July 2022, the Lobster Eye Imager for Astronomy (LEIA) pathfinder was launched, mounted on the SATech-01 satellite, which features MPOs in a 6×6 lobster eye configuration. The latest result shows that the design is performing as expected.²⁶

To facilitate accurate simulations of the SMILE SXI instrument, the optics parameters, CCD dimensions, and space radiation environment are based on an early version of the instrument design referred to as SXI 1.x. The parameters are listed in Table 1.

2.1 Optical Blocking Filter

Due to the design of the MPOs and lobster eye instruments, a straight-through solid angle is present for particle trajectories. Therefore, instruments using this type of optic may see a higher level of optical stray light or increased background, and additional optical blocking filters (OBFs) are thus required, possibly more than for previous X-ray instruments due to the much larger field of view. The OBF can either be affixed directly to the CCDs as is common in non-MPO designs or be deposited directly onto the MPOs. The OBF is adhered to the front surface of the MPO,

facing the radiation source. Due to the necessity of the OBF when using this type of optic, this paper will also explore the effects of an aluminum OBF on doses by altering its placement within the instrument. An OBF deposited directly onto the detector surface, referred to as on-chip, has been compared with OBF placements on the front or back of the MPOs.

3 Radiation Environment

The radiation environment in space varies based on the mission orbit and location. Radiation damage to CCDs is normally attributed to three key sources: galactic cosmic rays (GCRs), solar particles, and trapped particles. The latter is important for orbits that are in or pass through planetary body radiation belts, whereas GCRs and solar particles are present in all orbits, but their intensity is dependent on the orbit and solar activity. For example, the solar particle intensity is lowered in low Earth orbit (LEO) due to the protection from the Earth's magnetic field. GCRs consist of mostly ions from sources outside the solar system. The majority of the GCR ion spectrum is formed of protons (89%) with alpha particles accounting for $\sim 10\%$, and the remainder are heavier ions.²⁷ The higher mass particles interact with the spacecraft and scatter, producing showers of secondary particles that can cause transient energy deposits in the CCD or can lead to permanent effects such as displacement damage.

The SMILE SXI 1.x mission has a highly elliptical orbit and will be subject to different radiation environments along its path. The mission will be exposed to trapped proton, trapped electron, GCR, and solar particle environments. The SMILE SXI has a radiation shutter door that closes under a few scenarios. For the results presented in this paper, it is assumed that it only closes below a specific altitude to protect it from trapped particle radiation. Therefore, trapped particle radiation dose contributions are only applied along this section of the orbit when the door is closed.

3.1 Solar Energetic Particles

The Sun is also a large source of radiation that emits a steady stream of protons and electrons via the solar wind. The lower bound of the energy spectra is on the order of a few electron volts, which is much lower than other particle sources such as GCRs. For the lower energy domain of the solar particle spectra, minimal shielding will mitigate against it. However, the Sun can also emit higher energy particles with a high flux from coronal mass ejections (CMEs) and solar flares. These particles are referred to as solar energetic particles (SEPs), and the majority of these particles are protons. Due to their low energies, SEP trajectories can be altered by instrument optics systems such as MPOs and thus become focused and cause additional damage.

Because SEP events are probabilistic phenomena, they are difficult to model; thus, current models predict the flux with an associated confidence level to account for this probabilistic nature. The Emission of Solar Protons and Prediction of Solar particle Yields for Characterizing Integrated Circuits (ESP-PSYCHIC) model is recommended by the ECSS-E-ST-10-04C²⁸ standards, and this model will be used for sectoral analysis dose calculations in this paper. However, during the studies, it was identified that the ESP-PSYCHIC model has an issue with its low-energy spectrum. The predicted flux of the ESP-PSYCHIC model decreases with confidence level; this is shown in Fig. 2, with the key inflection point marked with a red-dotted line at 0.163 MeV/nucleon. The cause of the inflection was identified from the SPace ENVironment Information System (SPENVIS) documentation²⁹ and is due to the amalgamation of two separate models: ESP and PSYCHIC. These are coupled together using scaling factors, and the lower bound is at 0.173 MeV/nucleon, marked as a green line in the figure. Therefore, below 0.173 MeV/nucleon, the scaling factors may not alter predicted fluence. Figure 2 exhibits the evidence for this feature, and as the confidence level increases, the flux decreases below 0.163 MeV/nucleon. This will cause the dose from low-energy protons ($\lesssim 200$ keV) to be under-predicted for increasing confidence levels. This lower energy range is important as bulk damages to silicon detectors occur, and peak damage occurs around 100 keV.³⁰ Consequently, for regions with minimal aluminum equivalent thickness shielding, this will be an issue as the dose would likely be higher. Thus, this will affect the sectoral analysis approach for unfocused dose calculations that use depth dose curves from SPENVIS.

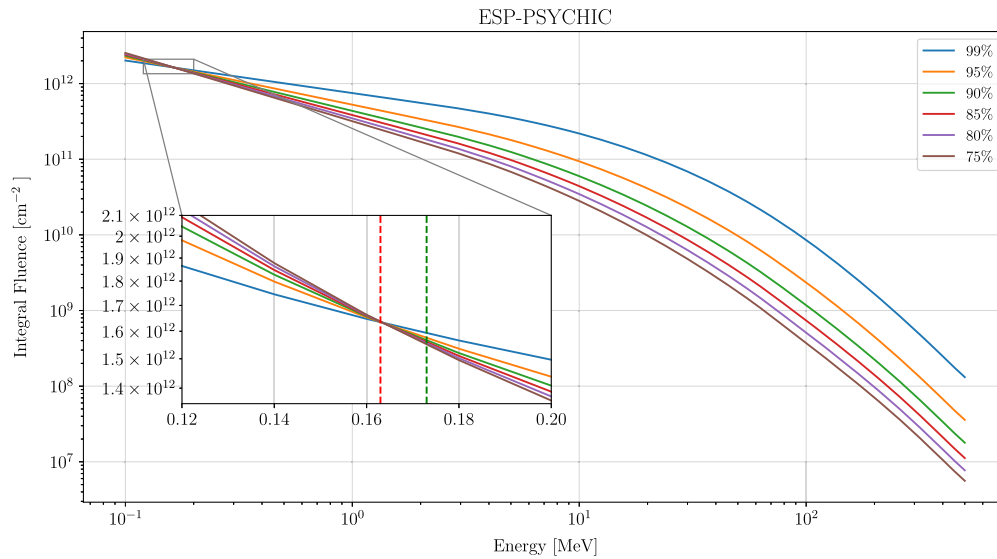


Fig. 2 ESP-PSYCHIC confidence level issue. The inflection point is marked with a red dashed line at 0.163. The green dashed line indicates the energy (0.173 MeV/nucleon) where the scale factors in the model start. Therefore, the model extrapolates for energies below this point. For the solar protons shown, the nucleon number is one.

The depth is defined from the outer surface inward to the center of the volume. Due to the inflection observed in the ESP-PSYCHIC model, experimental time-series data were used as an alternative representation of the SEP spectra. An Advanced Composition Explorer - Electron, Proton and Alpha Monitor (ACE-EPAM) dataset from 1997 to 2013 (ACE-EPAM data provided by Nicholas E. Thomas of the University of Maryland Baltimore) was used. The data for ACE-EPAM and ESP-PSYCHIC are compared in Fig. 3. The flux for the ESP-PSYCHIC models was calculated at 95% confidence and shows an agreement with the 95th percentile range of the ACE-EPAM time-series derived data as expected. Depth dose curves for the ACE-EPAM were produced using the SHIELDOSE-2 and non-ionizing energy loss for simple geometrical tools in SPENVIS. Both the ESP-PSYCHIC and ACE-EPAM dose contributions are compared for the SSA of the unfocused dose. For Monte Carlo simulations of the focused dose, only the ACE-EPAM time series is sampled and used to seed all simulated particle spectra.

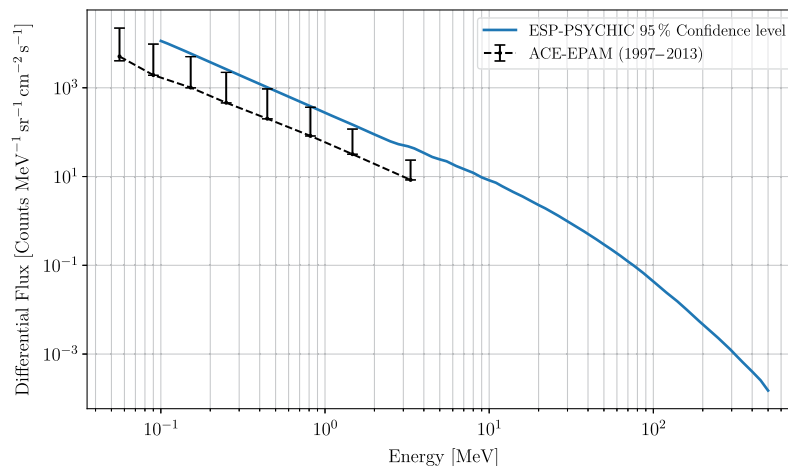


Fig. 3 Average flux measurements from a variety of models and datasets. The ACE-EPAM error bars represent the 5th and 95th percentile ranges. The ESP-PSYCHIC models were taken from SPENVIS estimates for highly elliptical orbital parameters similar to those planned for the SMILE mission.

4 Dose Calculation Methodology

All simulations performed for the studies within this document are built using the Geant4 Monte Carlo (MC) toolkit that provides code for the transport of particles through matter.³¹ Version 10.3.3 of Geant4 was used for the simulations with a modified version of the QBBC physics list. This reference physics list includes both the binary cascade and Bertini cascade models and is recommended for use in space applications. The modifications include the Space Physics User List (SUPL),³² replacing the default electromagnetic physics list used in QBBC. For the Advanced Telescope for High Energy Astrophysics (Athena) mission, the SUPL was developed as part of the Athena Radiation Environment Models and X-Ray Background Effects Simulators (AREMBES) study. The physics list has been validated against Geant4 versions 10.3 and 10.4 and has been used to study the instrument background for space instrumentation.^{33–35} Further modifications have been made to the physics list to include the Auger effect and Particle-induced X-ray emission (PIXE). It should be noted that this physics list differs from the *Space Physics List* included in the advanced examples released in Geant4 11.2.

Simulations can be created using Geant4 to assess the dose for a single instrument or full spacecraft. The toolkit enables many properties of particles to be tracked and recorded, such as the path length through the material and subsequent energy depositions. The toolkit also allows for ray tracing calculations to be implemented, enabling sectoral shielding analysis (SSA) to be performed. SSA is a simple and effective method of producing dose estimates for a spacecraft without running a full-scale MC simulation including particle interactions and trajectories. Two key components required for SSA are a mass model and depth dose curves. The mass models are derived from the full computer-aided design (CAD) models of the spacecraft, are comprised of simplified geometry objects, such as cubes and cylinders, and are representative of the original spacecraft for particle transport calculations. The depth dose curves are produced based on the orbital information for the mission using tools such as SPENVIS and Outil de Modélisation de l'Environnement Radiatif Externe (OMERE), with the depth dose curves then providing the dose for an equivalent aluminum shielding thickness. The dose, D , is then estimated by combining the dose from equivalent aluminum thicknesses $d(x_i)$ with the corresponding solid angle Ω_i that the thickness represents, which is calculated as

$$D = \sum_i d(x_i)\Omega_i. \quad (1)$$

Ray tracing is used to calculate the effective thicknesses from mass models by measuring track length and material properties, as depicted in Fig. 4. This SSA method is commonly used for dose estimates as it produces values that are representative of full Monte Carlo simulation without the central processing unit (CPU)/time overheads.

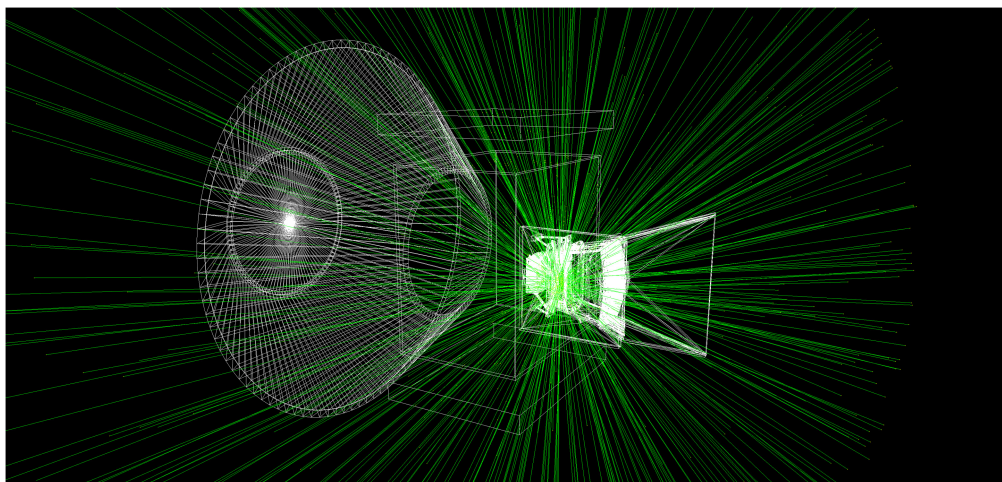


Fig. 4 Demonstration ray tracing through a physical model of SMILE SXI and spacecraft representative volumes to generate aluminum equivalent shielding histograms. The data from this technique are combined with depth dose curves to calculate a dose.

Missions that include focusing X-ray optics can focus radiation sources, which increases the background. As the SSA estimates do not include scattering effects, they are not representative of the solid angle of the optics or the additional background that they produce. Therefore, SSA represents the unfocused dose component caused by high-energy particles such as GCRs.

High-energy particle sources such as GCRs will pass through the optics and not be focused toward the focal plane. Lower energy particles that would normally not pass through the spacecraft shielding can pass through the optics via either scattering or passing straight through. The focused dose is therefore dependent on the particle flux spectra from these low-energy sources. A lobster eye optic, similar to those used on SMILE and planned for THESEUS, would focus solar energetic particles onto the instrument, providing an additional dose component. Two simulation techniques for the estimation of the focused dose from MPOs are now explored and will be compared with the focused dose estimates from SSA.

4.1 Segmented Technique

The segmented technique uses many justifiable approximations to create a simplified version of the lobster eye optic. The MPOs that form the lobster eye optics are approximated to be made of large area flat panels that form the curved surface in the (θ, ϕ) axes, as shown in Fig. 5(a). Using equal angles in θ and ϕ creates square segments. Due to the symmetries of the lobster eye over the detectors, only a quadrant of the optics is required to be simulated, as depicted in Fig. 5(b),

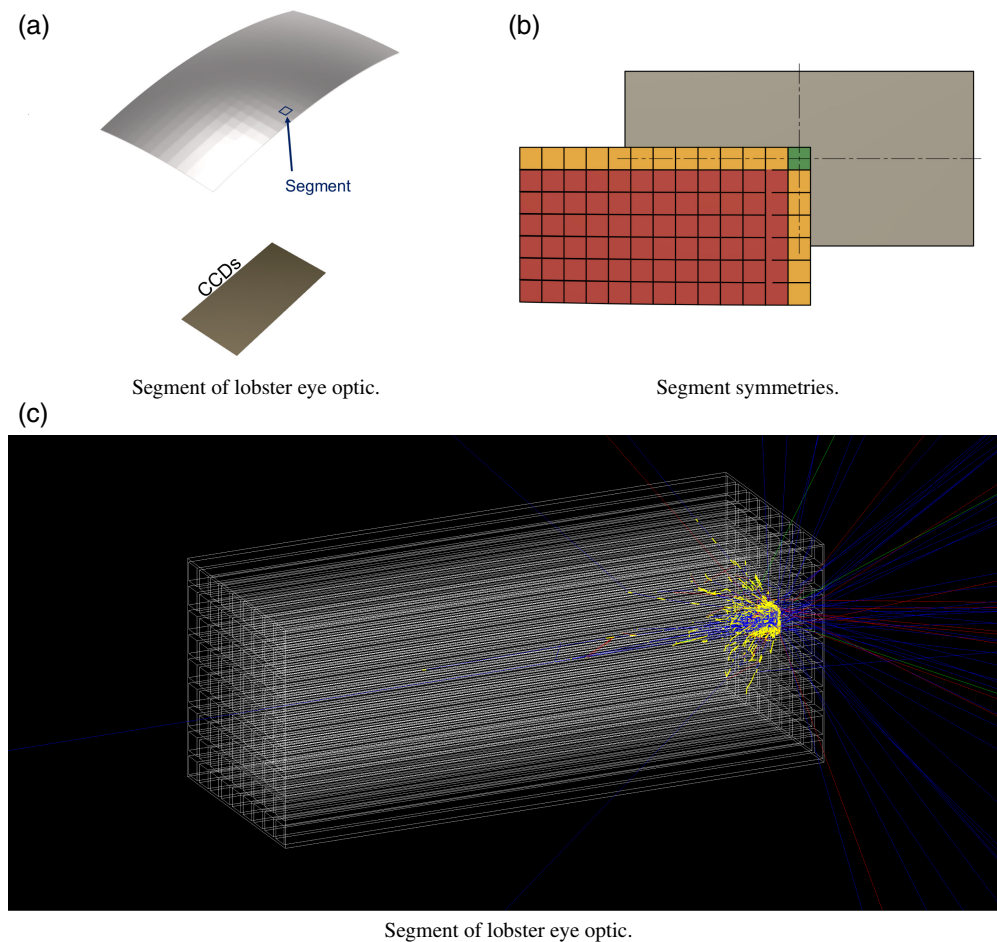


Fig. 5 Segmented geometry simulation setup. The track color represents the charge of the particles. Positively charged particles, mainly protons with some positrons, are blue, and negatively charged particles, consisting primarily of electrons, are red. Green tracks represent photons and other neutral charge particles. Interactions between the particles and geometry are shown as yellow points.

reducing the CPU time required for the simulation by a factor of 4. A quadrant represents a 2×4 MPO unit, whereas the whole SMILE SXI optic is formed of two 4×4 MPO units.

Reflecting the data generated from the quadrant can be used to create a full-dose map across the focal plane. Data from the yellow segments require one reflection, whereas those in red are reflected multiple times to construct an image. However, to achieve unique variations in each quadrant, four simulations need to be combined. This removes patterns caused by mirroring the data to achieve a full-dose map. The MPO pores are simulated using the `G4_GLASS_LEAD` material in the Geant4 NIST compound database. It should be noted that the iridium coating was not included in these simulations to simplify the geometry.

To simplify the model, each simulated square MPO segment is flat, and the curvature comes from the rotation of each mirror segment unlike the flight MPOs, which will have an internal curvature. For a segment, it is assumed that the dose contribution and CCD interaction location from a particle traveling through a pore is the same for the whole segment. This approximation is made to reduce the complexity. Therefore, only a small array of the MPOs is simulated in the center of the segment, as shown in Fig. 5(c). This approximation has the added benefit of removing any potential edge effects from the flat segments overlapping to produce the MPO curvature. The size of the central MPO array can also be altered to improve the focus of the segment. The segmented simulations presented in this paper use a 9×9 grid such that multiple scatters to the detector can be simulated, rather than a smaller 3×3 grid, which could lead to a proportion of particles not being focused toward the focal plane.

Particles are generated over the central pore, including the pore wall, with a Lambertian angular distribution to replicate the isotropic radiation sources in space. The simulation is performed in the frame of reference of the central pore, with the CCDs being rotated between simulations to replicate data from different MPO segments. Only the MPOs and CCD geometry objects are simulated.

The energy deposits, interaction positions, and additional information are recorded from the CCD-sensitive detector objects. This is post-processed with multiple normalizations applied to account for the approximations and to enable dose rates to be calculated. The total non-ionizing dose was calculated from non-ionizing energy loss (NIEL) in the simulation. This was achieved by backporting the `CalculateNIEL` function from the Geant4 10.7 source code. This Geant4 function is limited and only works for protons and alpha particles that deposit energy.

4.2 Full Pore Technique

The full pore method aims to simulate as many of the MPOs that form the lobster eye as possible for a more physically representative simulation. The geometry of each simulated MPO is built from many spherical segments and thus more accurately represents the mission-like MPOs. The MPO geometry of the full pore technique is shown in Fig. 6(a). Similar to the segmented method, `G4_GLASS_LEAD` is used for the MPOs, and the iridium coating was not included. Over 1.7×10^7 geometrical objects were created for the modeling of the SMILE SXI, which carries a computational overhead.

The particles are generated on a segment of a sphere and once again sampled from a Lambertian distribution to replicate the isotropic nature of particles entering the MPOs. Figure 6(b) displays an example of the particle generation region's validations using non-interacting special Geantino particles in Geant4. The particle generation region can be set to a quarter of the MPOs and uses symmetry approximations to reduce the CPU time, similar to the segmented technique.

Due to the simulation design modularity, additional masses can be added such as the optical blocking filter. In its default form, the simulation does not include additional masses and only includes aluminum and titanium base structures, with the glass MPOs and a silicon block representing the CCDs.

Similar to the previously described segmented technique, simulations of the energy deposits and interaction positions in the CCDs are recorded. The data is post-processed, and normalizations are applied where required. The post-processing stage is quicker in comparison with the segmented simulations as coordinate transformations are not required.

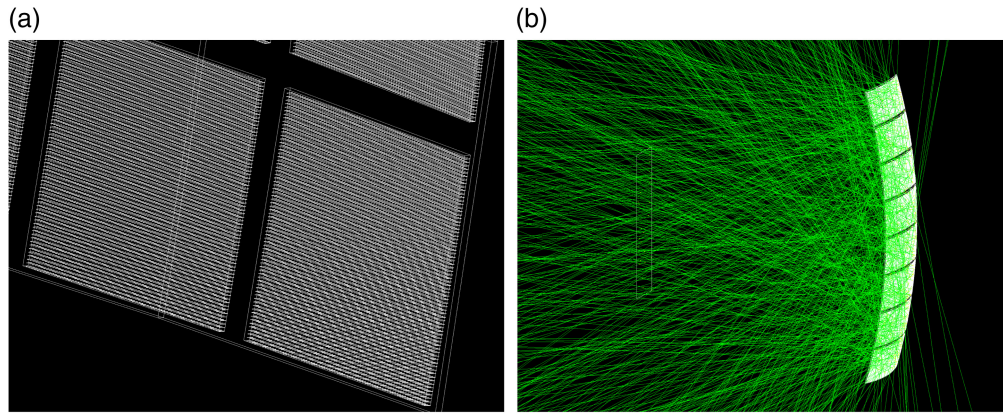


Fig. 6 Full pore detector construction geometry. The number of pores shown is reduced such that the visualization manager can display them on the screen. The low polygon count in the Geant4 visualization is not present in the simulation kernel, so there are no overlapping volumes. The particle generation direction samples from a cosine distribution that is used to replicate the isotropic distribution of particles in space. As shown in the image, some particles are directed away from the detector due to the curvature of the lobster eye optic. (a) Zoomed in view of MPOs. (b) Geantino particle generation tests.

5 Results and Discussion

The dose estimations from the unfocused SSA and focused Monte Carlo simulations are reported in this section, and a short summary table is provided in Table 2. The two focused dose simulations produce total ionizing dose (TID) and total non-ionizing dose (TNID) estimates for the SMILE SXI 1.x 3-year mission profile and are compared throughout the subsections. TNID calculations are given as displacement damage equivalent fluence (DDEF) for 10 MeV protons. The focused dose techniques are used for the dose mapping comparisons as the SSA technique for unfocused is not capable of this detail. The full pore technique was the only focused dose method for investigating the impact of the optical blocking filter position on the dose rate, due to its modular design.

5.1 Comparison of Models for Unfocused Dose

The SSA technique uses a depth dose curve from SPENVIS using a 95% confidence level. For the early spacecraft design concept phase for the SMILE mission, referred to as SXI 1.x, the unfocused radiation dose assessment that indicated the TID was 1.14 krad and TNID $2.3 \times 10^9 \text{ cm}^{-2}$ for 10 MeV equivalent protons, using the SSA method, with the ESP-PSYCHIC model.

Table 2 Summary overview of the different techniques for the dose estimations. A numerical output refers to a value estimating the total dose. A spatial output describes the dose across the detector volume.

Technique	Flux dataset	Dose output(s)	Short summary
SSA	ESP-PSYCHIC and ACE-EPAM	Unfocused dose. Numerical	Analytical formula that uses SPENVIS depth dose curves in combination with ray-traced paths through the spacecraft to estimate the unfocused dose.
Segmented	ACE-EPAM	Focused dose. Numerical and spatial	Geant4 simulation of a small MPO segment. Multiple simulations with the detector volume translated and rotated are combined together to represent a curved surface.
Full pore	ACE-EPAM	Focused dose. Numerical and spatial	Geant4 simulation of a complete MPO curved surface. Particles can be simulated over the whole area of the curved surface.

Table 3 These focused datasets use the ACE EPAM 2013 time series as input for SEP modeling, and their errors are based on simulation statistical results. The dose estimates are for a 3-year mission of SMILE SXI 1.x.

Technique	Segmented	Full pore
TID (krad)	0.2067 ± 0.0001	0.2041 ± 0.0001
TNID (cm^{-2})	$(3.754 \pm 0.007) \times 10^9$	$(3.916 \pm 0.002) \times 10^9$

The values are calculated from two separate mass models: one with the SMILE radiation shutter door closed and one with it open. It is assumed that the door is closed when passing through the trapped particle regions. When the door is open, only the SEP dose is calculated. The total dose presented in the calculated values is calculated with summed weightings based on the expected door closure time. These predicted dose values do not include the impact of GCR and their resultant secondaries, and this is typical with SSA.

The ACE-EPAM data was also used to predict the SEP dose for the unfocused scenario. The input spectra have a maximum input energy of 4.75 MeV. The dose estimate using ACE-EPAM-based depth dose curves returned zero doses for both open and closed models. This is because the energies and associated particle fluences were not high enough. The ESP-PSYCHIC was also cut down to a 4.75 MeV maximum energy and returned a zero dose, validating the energy relation (Table 3).

5.2 Comparison of Focused Dose Techniques

The two focused dose techniques were used to calculate the dose for a lobster eye optic using the parameters listed in Table 1. The errors are based on the simulation statistics used. They do not include approximation or systematic uncertainties. In the absence of experimental data for validation, the data does reveal the same order of magnitude that is observed for the two techniques.

The segmented simulation is faster than the full pore simulation; however, it requires post-processing to perform coordinate transforms. The total time of simulation and analysis for the segmented technique is longer than that of the full pore technique. Code optimization of the post-processing would likely make the segmented technique quicker overall. Therefore, for larger MPO structures, this presents an alternative approach with a reduced simulation time and resource complexity.

5.3 Focused Versus Unfocused Dose

The unfocused results, which use the ESP-PSYCHIC SEP model, are used for comparison in Sec 5.3 despite the issues already identified with the confidence levels with the model. The reason for this choice is that it is more representative of the full-duration mission. That includes periods of increased SEP rates from solar activity and has a wider energy range. This leads to unfocused dose predictions that are non-zero. The ACE-EPAM data are being used for the focus as they are more representative of the day-to-day SEP rates. When the SEP rate is up, the radiation shutter door will be closed to protect the CCDs, and the focused dose component will be mitigated against.

The results show that the focused dose corresponds to $\sim 15\%$ of the combined focused and unfocused dose components for the TID, and the focused dose represents the TNID $\sim 63\%$ of the combined dose. Therefore, this highlights the importance of considering both the focused and unfocused doses for missions that include lobster eye MPO X-ray optics. Breaking down the unfocused TID into components shows that the SEPs contribute 0.898 krad and 90% comes from the open-door position. The same is observed for TNID. The dose contribution from low-energy particles is missed by the SSA unfocused calculations, due to the dose depth curves as previously demonstrated.

For the SMILE SXI version 1.x design, parameters and radiation environment were used to create the data for the unfocused and focused doses. The CCDs would be below the dose limits for a 3-year mission. However, increases to 5 years and beyond would not be advisable when including the focused dose. Thus, this shows the importance of including the focused dose

component in which the instrument operation for science returns is dependent on dose. If the focused optical estimates are accurate, then nearly two-thirds ($\sim 63\%$) of the TNID dose arrives via the MPOs. This further highlights the importance of considering the focused dose component for instrumentation that incorporates MPOs.

5.4 Focused Dose Distribution

Both simulation techniques enabled the dose to be mapped across the CCD area. The two-dose maps for TID are shown in Fig. 7. The data show that the segmented technique produces a mostly uniform dose with the dose decreasing around the outer edges of the CCDs. By design, the segmented technique only simulated a few locations, which contributes to the uniformity. By contrast, the full pore produces a uniform dose with more noise across the device with an “ ∞ ” pattern subtly observable in the data. The greater noise can be partly attributed to lower simulation statistics.

The full pore method was simulated twice with different particle generation regions: once with the full lobster eye optic area, representing the two 4×4 MPO units and once for a quarter representing 2×4 MPO units. The same “ ∞ ” pattern was observed in both simulations and in repeats of the simulations. Therefore, this pattern is not an artifact resulting from only simulating a quarter of the full optic area. Geometry of overlap checks was performed in Geant4, which ruled out a geometry error causing the artifact. Therefore, it is suspected that the “ ∞ ” pattern is due to the focusing of the simulated particles. The central ellipse was more circular when the MPO material was changed from lead glass to silicon during an investigation study. The patterns

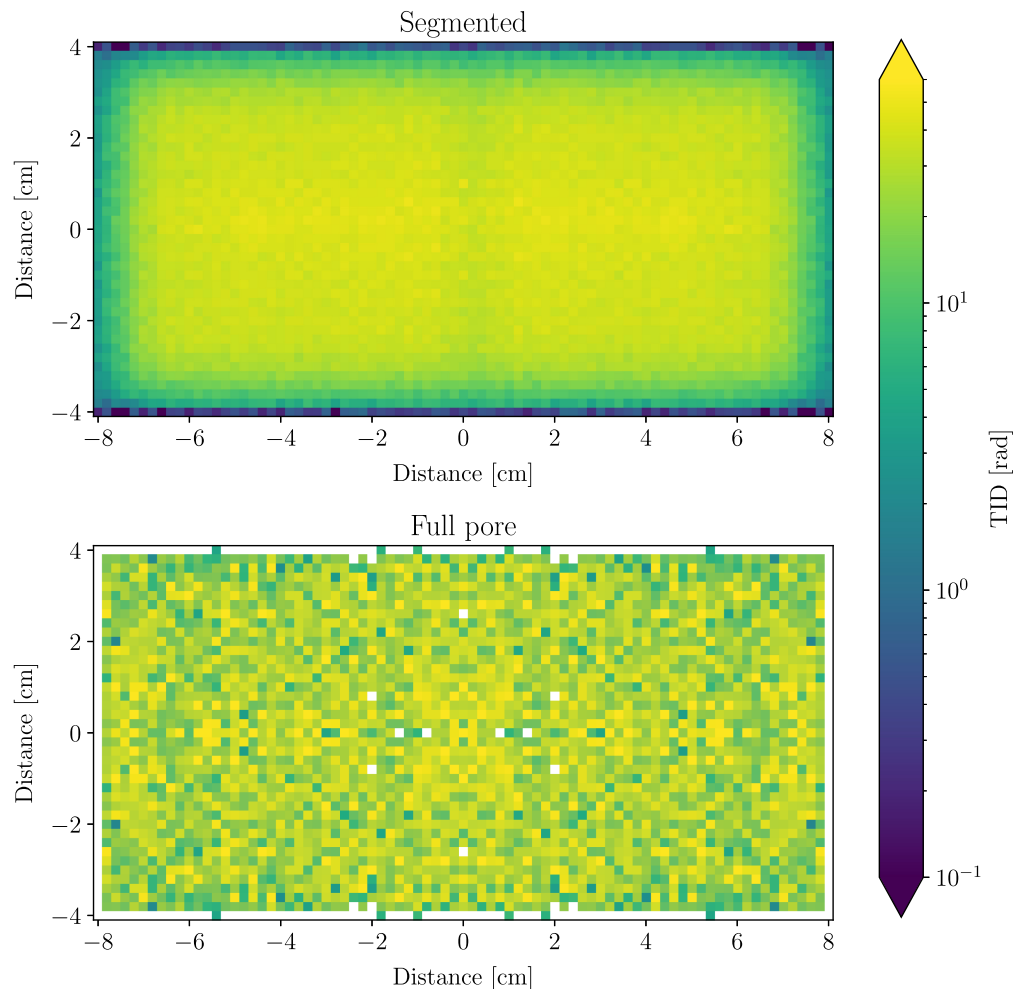


Fig. 7 Segment and full pore simulation TID positional map comparisons. The segmented technique was simulated with more data, and hence, the data is less noisy.

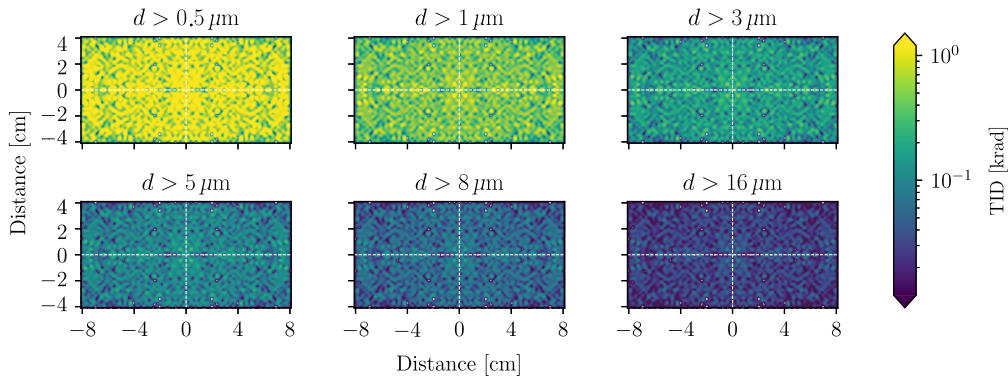


Fig. 8 Depth profiles of TID of full pore simulation. The four quadrants are marked to show the rough reflection points for the singular dataset.

have also been observed to alter with changes to the radius of curvature of the lobster eye optic and changes in the MPO properties: pore width, wall width, and pore length.

The dose maps for the full pore method were analyzed at different depth cuts, where the depth is defined from the top surface of the device, i.e., the entrance window of the sensor. These are shown in Fig. 8. The cuts show the patterns and reveal that they become less refined the deeper into the CCDs the cuts are performed.

Understanding the dose depth profile is crucial for devices such as CCDs, particularly in relation to the depth at which charge is stored and transferred within the devices. A key metric of CCDs, charge transfer inefficiency, is significantly degraded by charge trapping as a result of TNID. Therefore, the dose depth profile, and hence the level of charge trapping within the CCD buried channel, is key to accurately determining the effect on the CCD performance. The buried channel is located toward the bottom surface of the device.

The dose map depth cuts demonstrated that the dose reduces the deeper into the silicon the cuts are made. Figure 9 shows the plots for both TID and TNID with depth through the CCDs. The plots also compare the segmented and full pore simulations, with the two techniques showing good agreement with the distribution of doses. The top surface of the CCDs experiences the highest TID. This is where many low-energy particles are absorbed into the silicon. The dose drops below 0.2 krad at depths of 5 μm and below. Therefore, ionizing dose damage effects are most likely to cause issues at the top of the detector silicon. The buried channel is near the bottom of the device, and the damage occurs near the top. Therefore, due to the damage proximity from the buried channel, it leads to less of an operational impact than if it occurred deeper into the detector's silicon.

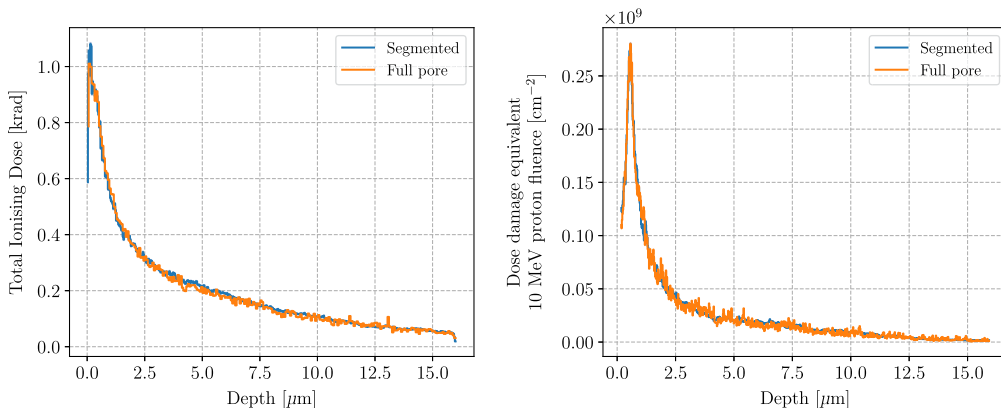


Fig. 9 Depth dose comparison between the two simulations. The left side shows the agreement for the TID. The right side shows the TNID. It should be noted that the upper and lower bins of the TNID data are not included in the data presented due to a boundary problem in the TNID calculation used.

Table 4 Total ionizing dose and total non-ionizing dose for different optical blocking filter configurations using the geometry method simulation. The error on the TID values is $\sim 1 \times 10^{-4}$ krad. The TNID has errors with an order of magnitude of $\times 10^7$ cm⁻².

OBF configuration	No OBF	On-chip	Rear of MPOs	Front of MPOs
TID (krad)	0.204	0.200	0.195	0.203
TNID (cm ⁻²)	3.92×10^9	4.13×10^9	3.50×10^9	3.89×10^9

By contrast, the TNID is highest at a subsurface depth of 0.8 μ m. The heavier particles attributed with TNID have to travel a distance into the material before they are attenuated. The majority of the particles contributing to the TNID are from the SEP protons, rather than their secondary particles. It should be noted that the two surface bins were removed from the TNID plot as these have extremely high doses that are attributed to a boundary problem in the simulation, which is not physical.

The dose depth profiles demonstrate that different degradations of the sensor could occur depending on whether a front- or back-illuminated device is used. Detailed modeling of the operation of CCD or CMOS devices with the energy deposits would determine the specific impact.

5.5 Optical Blocking Filter Configurations

The impact of the MPO OBF location on the TNID and TID was investigated. An aluminum OBF with a 100 nm thickness was simulated in three locations: on-chip (CCD), on the rear surface of the MPOs, and on the front surface of the MPOs (standard position). For the MPO OBF, the front surface is defined as the side of the MPOs facing the sky, and the rear surface is the side of the MPOs facing the detector.

Table 4 compares the TID and TNID between each setup. The simulation configuration without an OBF is used for comparison. All scenarios have a small reduction in dose from the simulated low-energy protons. When the OBF is on the front surface of the MPOs, the TID is the highest of all three OBF scenarios tested, and the results are the closest to without an OBF. Any particles generated from the front surface OBF will also be focused down, through the pores, onto the CCDs. The OBF on the rear surface of the MPOs was used to test this theory, in which any scattered particles from the OBF are not focused down toward the detector. This causes this OBF configuration to have the lowest TID and TNID. However, it should be noted that it is not currently mechanically feasible to affix the OBF to the rear side of the MPOs.

The on-chip configuration has the highest TNID of all three simulations. The higher dose is attributed to the production of low-energy secondaries produced from primary interactions with the OBF. Due to the particle species and energies of scattered lower energy secondaries produced, they are absorbed into the device increasing the TNID. Given the impact of dose on the operation of the CCD detectors for a mission such as SMILE, the TNID is more of a concern. Therefore, minimizing the TNID is key for increasing their operational lifetime, ruling out the on-chip OBF with the current thickness for the tested configuration. A thicker on-chip OBF could potentially reduce the TNID in this scenario. Thus, simulations would be required for the specific mission and OBF configuration used.

Placing the OBF on the MPO's front surface offers the best scenario given the manufacturing difficulties of an OBF on the rear surface of the MPO. Both MPO-based OBF configurations have the benefit that the MPOs act as another shield for the lower energy particles to be absorbed. A thicker OBF will also likely further reduce the TID result.

6 Conclusions

Throughout a spacecraft's operational lifetime, it will be exposed to the space radiation environment, which interacts with the spacecraft and causes damage, with image sensors such as CCDs and CMOS devices being particularly vulnerable. These are chosen and qualified for radiation level estimates for missions, and simulations are generated based on the specific orbital

parameters, which are then used to generate the dose depth curves. These dose depth curves are used in sectoral shielding analysis (SSA) to improve shielding and reduce the overall dose. The analysis also provides the expected radiation dose maxima for the mission. SSA is a ray tracing technique and does not include a full Monte Carlo treatment of radiation interactions and dynamics.

Several future space missions such as SMILE use lobster eye optics that are made up of tessellated MPOs. MPOs are made up of a series of microscopic pores that can have direct lines of sight from the radiation source to the imaging sensors on board. The MPOs will also focus a proportion of the incoming radiation onto the image sensors, leading to more damage. The SSA method does not include focusing effects and is more suited to higher energy particles that would transverse shielding and interact with image sensors. Solar energetic particles, specifically the protons, have energies that mean they will become focused by the MPOs.

The SSA unfocused dose estimates were performed with the ESP-PSYCHIC model for SEPs. It was noted that this model has issues below 200 keV, which is an important region relating to bulk damage to silicon detectors. A time series dataset that had a maximum energy of 4.75 MeV was also used for comparison. This predicted zero dose as there is sufficient shielding. However, the time series data do not account for flaring over the life of the mission. Therefore, despite the ESP-PSYCHIC issues, it was used for unfocused dose estimates. The time series data was used for the focused dose simulations as it is important to understand the radiation damage impact when the radiation shutter door is open. The radiation shutter door is closed during flaring, minimizing the radiation damage to the SMILE SXI CCDs.

Two Monte Carlo simulation methods for analyzing this focused dose component were investigated. The simulations used the Geant4 toolkit and were designed to include the ability to map the dose across the SMILE image sensors. The simulations differed in complexity, computational resource usage, and time. The focused simulations were compared with unfocused simulations that used the SSA method.

The total non-ionizing dose and the total ionizing dose predictions between the two Monte Carlo simulations produced similar estimates with the same order of magnitude.

The two focused dose Monte Carlo simulation methods enabled dose maps across the CCD volume to be generated. These revealed fairly uniform distributions across the image sensor volumes. The design of the full-pore simulation method revealed that patterns of slightly higher doses exist across the device. The patterns are due to the focusing effects of the protons, and the patterns were visible at various depth cuts through the image sensors. The depth dose across the devices decreased with the depth of the sensor. The TID was highest at the front surface, and the TNID was highest at approximately a micron into the sensor due to particle attenuation. These results show that impact on device operation could vary based on its internal working such as being front or back illuminated.

Focused TID and TNID were compared with unfocused doses for the SMILE SXI 1.x mission profile. It was shown that the focused dose contributed to a significant proportion of the combined total TNID and a smaller proportion of the TID. Therefore, evaluating focused doses during design stages is an important step in preventing devices from going beyond their operational dose design limits. These numerical values do not reflect those of the final mission at launch as they are based on an earlier design revision.

The position of an optical blocking filter and its impact on the focused dose were evaluated via the full pore simulation method. The simulations revealed that the largest reduction in TID and TNID occurred when the OBF was affixed to the MPOs compared with an on-chip OBF. An OBF affixed to the rear surface of the MPOs offered the best reduction in dose but is not currently feasible; therefore, the front MPO position offers the best location. Similar results were determined for the TNID; however, the TNID increased slightly when the OBF was affixed to the front side of the MPOs. Therefore, there are trade-offs in OBF location and focused dose, which will be mission-dependent.

In summary, all two focused dose methods appear to be able to predict the expected dose and show an order of magnitude agreement for TID and TNID. The results also demonstrate that the dose distribution profile could impact front- or back-illuminated devices differently due to their internal structures. The focused dose made up a significant proportion of the total overall estimates. The unfocused dose using SSA misses the day-to-day focusing of soft protons.

Code and Data Availability

All data in support of the findings of this paper are available within the article. The underlying raw data supporting the conclusions are not publicly accessible due to the data policies implemented by the respective missions. Interested parties may request the data from the authors; however, such requests will be subject to export control restrictions.

Acknowledgments

The authors would like to thank Nicholas E. Thomas of the University of Maryland Baltimore for initially providing the ACE-EPAM data source. Parts of the work presented were supported by grants covering the SMILE (UKSA, Grant No. ST/T003138/1), THESEUS (UKRI STFC, Grant No. ST/W000237/1).

References

1. W. Raab et al., “SMILE: a joint ESA/CAS mission to investigate the interaction between the solar wind and Earth’s magnetosphere,” *Proc. SPIE* **9905**, 990502 (2016).
2. H. Rauer et al., “The PLATO 2.0 mission,” *Exp. Astron.* **38**(1), 249–330 (2014).
3. S. Sembay et al., “The soft X-ray imager (SXI) on the SMILE mission,” *Earth Planet. Phys.* **8**(1), 5–14 (2024).
4. J. Endicott et al., “TreeView: a small satellite supporting precision forestry for nature-based solutions in a changing climate,” in *4S Symp.* (2022).
5. S. Sembay et al., “The soft X-ray imager (SXI) on the SMILE mission,” *Earth Planet. Phys.* **8**(1), 5–14 (2024).
6. L. Amati et al., “The THESEUS space mission: updated design, profile and expected performances,” *Proc. SPIE* **11444**, 114442J (2021).
7. P. Truscott et al., “Geant4—a new Monte Carlo toolkit for simulating space radiation shielding and effects,” in *IEEE Radiat. Effects Data Workshop. Workshop Rec. Held in Conjunction with IEEE Nucl. and Space Radiat. Effects Conf. (Cat. No. 00TH8527)*, IEEE, pp. 147–152 (2000).
8. F. Gastaldello et al., “A systematic analysis of the XMM-Newton background: IV,” *Exp. Astron.* **44**(3), 321–336 (2017).
9. R. Nartallo et al., “Low-angle scattering of protons on the XMM-newton optics and effects on the on-board CCD detectors,” *IEEE Trans. Nucl. Sci.* **48**(6), 1815–1821 (2001).
10. V. Fioretti et al., “Geant4 simulations of soft proton scattering in x-ray optics: a tentative validation using laboratory measurements,” *Exp. Astron.* **44**(3), 413–435 (2017).
11. F. Lei et al., “Update on the use of Geant4 for the simulation of low-energy protons scattering off x-ray mirrors at grazing incidence angles,” *IEEE Trans. Nucl. Sci.* **51**(6), 3408–3412 (2004).
12. L. Qi et al., “Geant4 simulation for the responses to X-rays and charged particles through the EXTP focusing mirrors,” *Nucl. Instrum. Methods Phys. Res. Sect. A: Accel. Spectrom. Detect. Assoc. Equip.* **963**, 163702 (2020).
13. J. Angel, “Lobster eyes as X-ray telescopes,” *Proc. SPIE* **0184**, 84–85 (1979).
14. M. R. Collier et al., “Invited article: first flight in space of a wide-field-of-view soft X-ray imager using lobster-eye optics: instrument description and initial flight results,” *Rev. Sci. Instrum.* **86**(7), 071301 (2015).
15. H. Chapman, K. Nugent, and S. Wilkins, “X-ray focusing using square channel-capillary arrays,” *Rev. Sci. Instrum.* **62**(6), 1542–1561 (1991).
16. G. Fraser et al., “X-ray focusing using square-pore microchannel plates first observation of cruxiform image structure,” *Nucl. Instrum. Methods Phys. Res. Sect. A: Accel. Spectrom. Detect. Assoc. Equip.* **324**(1–2), 404–407 (1993).
17. R. Hudec and C. Feldman, “Lobster eye X-ray optics,” in *Handbook of X-Ray and Gamma-Ray Astrophysics*, C. Bambi and A. Santangelo, Eds., pp. 1–39, Springer Nature, Singapore (2022).
18. R. Willingale et al., “Aberrations in square pore micro-channel optics used for x-ray lobster eye telescopes,” *Proc. SPIE* **9905**, 99051Y (2016).
19. C. Feldman et al., “The development of the THESEUS SXI optics,” *Proc. SPIE* **11444**, 114448X (2021).
20. K. Doi et al., “Ultrathin and lightweight lobster eye optics formed into a single flat substrate,” *Proc. SPIE* **11108**, 111080V (2019).
21. G. Branduardi-Raymont and C. Wang, *The SMILE mission*, pp. 1–22, Springer Nature, Singapore (2022).
22. E. Bunce et al., “The bepicolombo mercury imaging X-ray spectrometer: science goals, instrument performance and operations,” *Space Sci. Rev.* **216**, 126 (2020).
23. C. H. Feldman et al., “Calibration of a fully populated lobster eye optic for SVOM,” *Proc. SPIE* **11444**, 114441K (2020).

24. B. Walsh et al., “The lunar environment heliospheric X-ray imager (LEXI)—a mission for global magnetospheric imaging,” in *AGU Fall Meeting 2020 SM029-01* (2020).
25. W. Yuan et al., “The Einstein Probe Mission,” *Handbook of X-ray and Gamma-ray Astrophysics*, C. Bambi and A. Santangelo, Eds., Springer Living Reference Work (2022).
26. Z. X. Ling et al., “The lobster eye imager for astronomy onboard the SATech-01 satellite,” *Res. Astron. Astrophys.* **23**, 095007 (2023).
27. V. Bothmer and I. Daglis, *Space Weather: Physics and Effects*, Springer Praxis Books, Springer Berlin Heidelberg (2007).
28. “Space engineering: space environment,” <https://ecss.nl/standard/ecss-e-st-10-04c-rev-1-space-environment-15-june-2020/> (2020).
29. SPENVIS, “Help: solar proton models: the ESP models,” <https://www.spennis.oma.be/help/background/flare/flare.html#ESP> (accessed 2021-03-28).
30. B. K. Dichter and S. Woolf, “Grazing angle proton scattering: effects on Chandra and XMM-Newton X-ray telescopes,” *IEEE Trans. Nucl. Sci.* **50**(6), 2292–2295 (2003).
31. J. Allison et al., “Recent developments in Geant4,” *Nucl. Instrum. Methods Phys. Res. Sect. A: Accel. Spectrom. Detect. Assoc. Equip.* **835**, 186–225 (2016).
32. P. Dondero and A. Mantero, “A ‘Space Dedicated’ GEANT4 physics list from the AREMBES project,” in *12th Geant4 Space Users Workshop* (2017).
33. V. Ivanchenko et al., “Validation of Geant4 10.3 simulation of proton interaction for space radiation effects,” *Exp. Astron.* **44**(3), 437–450 (2017).
34. T. Eraerds et al., “Enhanced simulations on the athena/wide field imager instrumental background,” *J. Astron. Telesc. Instrum. Syst.* **7**(3), 034001 (2021).
35. M. Hubbard et al., “The CCD instrument background of the SMILE SXI,” *Earth Planet. Phys.* **8**(1), 1–10 (2024).

Michael W. J. Hubbard is a space radiation environment scientist at the Center of Electronic Imaging (CEI) at the Open University, United Kingdom. He assesses the potential radiation environment for future space missions and models the subsequent impacts such as dose and instrument background rates. His expertise revolves around the design of Geant4 simulations and data analysis pipelines for radiation detectors. He has a background in scintillation detector technology utilizing pulse shape discrimination for neutron detection.

Thomas W. Buggiey is a postdoctoral researcher in the Center for Electronic Imaging at the Open University, United Kingdom. His research interests include silicon pixel detectors (CCD and CMOS) as well as new technologies such as space-based X-ray interferometry. A significant amount of his work is carried out as part of large ESA and NASA space telescopes.

David Hall is a senior lecturer in physical sciences at the Open University, United Kingdom. Over the last 15 years, he has worked on the simulation of radiation environments, radiation dose, and impact in detectors and instrument background, studying the background on XMM-Newton, Swift, and Suzaku. He is currently involved in the background predictions for the SMILE and THESEUS SXI instruments alongside the Athena WFI, particularly the study of graded-Z radiation shielding and the validation of Geant4 for instrument background simulations.

Steve Parsons is a detector scientist at the Center of Electronic Imaging (CEI) at the Open University, United Kingdom. His work is currently focused on running a variety of test campaigns for the SMILE SXI CCDs, which includes both the radiation damage and pre-launch characterization of flight devices. He has a broad range of detector experience from the X-ray regime to the radio.

Biographies of the other authors are not available.